Paper 131

©Civil-Comp Press, 2012
Proceedings of the Eighth International Conference
on Engineering Computational Technology,
B.H.V. Topping, (Editor),
Civil-Comp Press, Stirlingshire, Scotland

# A Numerical Study of the Effects of Aerofoil Shape on Low Reynolds Number Aerodynamics

**H. Aono, T. Nonomura, M. Anyoji, A. Oyama and K. Fujii**
**Institute of Space and Astronautical Science**
**Japan Aerospace Exploration Agency**
**Sagamihara, Kanagawa, Japan**

## Abstract

A numerical study of the effects of airfoil shape on low Reynolds number aerodynamics is presented. The large-eddy simulations are performed with $6^{th}$-order compact finite difference scheme and $10^{th}$-order low pass filter, and $2^{nd}$-order backward implicit time integration with inner iterations. Systematic numerical excesses show the feasibility of the current simulations to predict flow fields around fixed-wing configurations involving a laminar separation and laminar-to-turbulence transition at low Reynolds number. At the Reynolds number of $2.3\times10^4$, two types of thin and asymmetric airfoils as a target airfoil shape of micro-size air vehicle are considered. The results show that the airfoil cross section affects the formation of a laminar separation bubble and the transition to turbulence in the three-dimensional flow around the wings at low angle of attack and hence significant influence on the aerodynamic performance.

**Keywords:** implicit large-eddy simulation, low Reynolds number flow, laminar separation bubble, transition

## 1 Introduction

Interest in micro air vehicles (MAVs) has grown noticeably encouraged by the miniaturization and battery of technology and the advancements in micro systems. The potential benefits of those vehicles for civil, military, and search and rescue operations are numerous.

As we design MAVs, several prominent features are identified: (i) low Reynolds numbers (i.e. $10^3$-$10^5$), resulting in degraded aerodynamic performance, nonlinear response to variation of angle of attack of the wing, and massive flow separation at high angle of attack; (ii) small physical dimensions, leading to much reduced payload capabilities, and some favourable scaling characteristics including structural strength, reduced stall speed, and impact tolerance; and (iii) low flight speed,

resulting in an order one effect of the flight environment such as wind gust, and intrinsically unsteady fight characteristics [1, 2, 3]. For the MAVs generally two types of propulsive system are considered: (i) fixed wing-based system (that requires additional resources of propulsion); and (ii) moving wing-based system (that can generate propulsive forces by itself). It is well-known that commercial airplanes employ the fixed wing-based system, helicopters the rotating wing-based system, and biological flyers the flapping wing-based system. Although favourable flight performance of moving wing based micro-sized air vehicles is to be expected, the current state of the art and the knowledge of flapping and rotating wings learned from natural flyers and helicopters is still challenging to apply in the vehicle design because of the complicity of the problems. Therefore current study focus on a fixed-wing and aerodynamics associated with it at low Reynolds numbers.

Figure 1 shows how a decrease of the Reynolds number affects the aerodynamic performance of represented airfoils. It is clearly observed that the lift-to-drag ratio substantially decreases as the Reynolds number decreases. The observed aerodynamic characteristics are associated with the laminar-turbulent transition process. For conventional aircraft wings, of which Reynolds numbers exceed $10^6$, the flows surrounding them are typically turbulent and the sufficient momentum is provided in the near wall region by turbulent mixing. Consequently flow separation is not encountered until the high angle of attack. For low Reynolds number fluid physics, the flow around the airfoil is initially laminar and is prone to separate even under a mild adverse pressure gradient. Under certain circumstances, the separated flow reattaches and forms a laminar separation bubble (LSB) while transitioning from a laminar to a turbulent state. Laminar separation can change the effective shape of an airfoil and consequently influence the aerodynamic performance [2, 4].

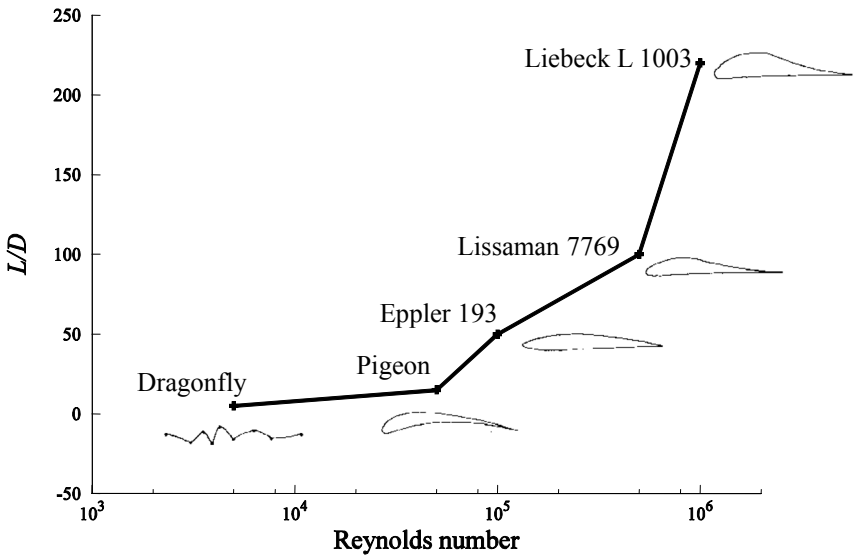


Figure 1: Aerodynamic characteristics of representative airfoils. Plot data are from Lissaman [4].

Therefore, it is essential to understand the behaviour of laminar separation on an airfoil in order to attain high aerodynamic performance at low Reynolds numbers. Furthermore, detail of afore-mentioned features is expected to be varied with the change of airfoil cross sections, orientation, and flow condition.

The objective of the current study is threefold: (i) to present the feasibility of numerical simulations to predict flows around fixed-wing configurations involving laminar separation and laminar-to-turbulence transition; (ii) to understand the impacts of the airfoil cross section on the formation of an LSB and the transition to turbulence in the three-dimensional flow around infinite wings at several angles of attack and at the Reynolds number of $2.3\times10^4$; and (iii) to elucidate the correlation between resulting aerodynamic performance and flow fields.

# 2 Case Statement

We select the chord- and freestream-based Reynolds number of $2.3\times10^4$ where small-scale air vehicles are operated in the Reynolds number range. As shown in Figure 2, we consider two types of airfoil shape: one is an Selig-Donovan (SD) 7003 airfoil [5, 6] (see Figure 2 (a)) and another is an Ishii airfoil (see Figure 2 (b)) [7]. A common characteristic of airfoil shape is asymmetric with a positive curvature of a lower surface of the airfoil. The SD7003 airfoil is designed for low bubble drag at low Reynolds numbers. Flow past the SD7003 airfoil and wing have been often considered as a research topic for different numerical and experimental studies since it exhibits an LSB on the upper surface that is present over a wide range of Reynolds numbers and angles of attack. On the other hand, the Ishii airfoil is designed by Mr. Ishii who has a world record of endurance time of non-propulsive flight. As seen in

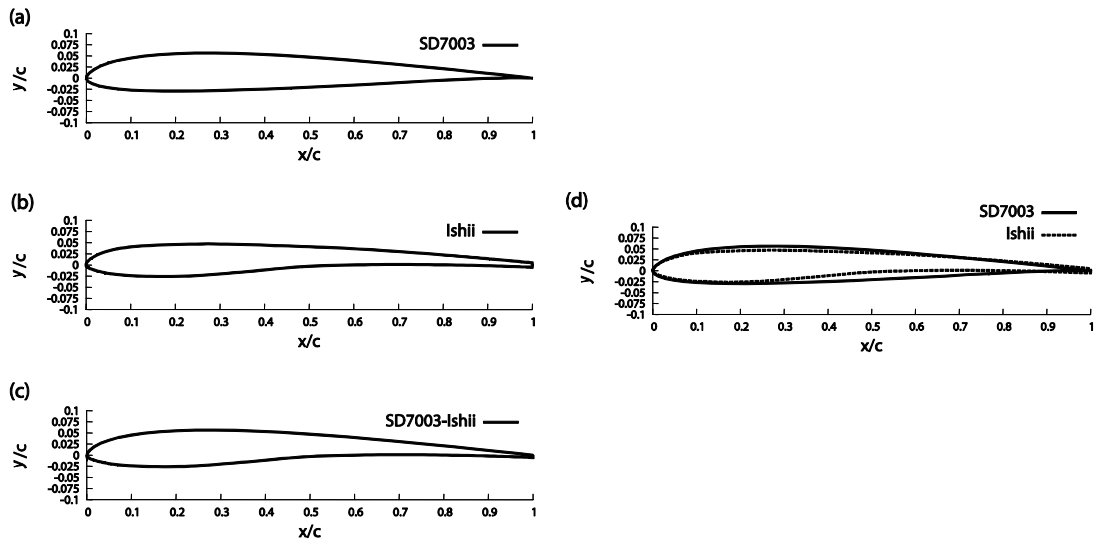


Figure 2: Images of airfoil shapes: (a) an SD7003 airfoil; (b) an Ishii airfoil; (c) a virtual airfoil (an SD7003-Ishii airfoil); (d) a comparison between SD7003 and Ishii airfoil.

Figure 2 (b) it has a unique profile of cross section and consists of relatively flat upper surface and greater positive curvature of a lower surface as well as sharp leading edge. It is interesting to note that the cross-sectional shape of the Ishii airfoil looks similar to that of the Pigeon as shown in Figure 1. In addition to two airfoils, we further consider a virtual airfoil shape that is built based on the upper surface of SD7003 airfoil and the lower surface of Ishii airfoil (see Figure 2 (c)). Although we cannot completely investigate individual effect of the upper and lower airfoil shape on the aerodynamic performance, we believe that this virtual airfoil could offer useful insights in our view.

We analyse instantaneous and phase-averaged flows fields around three airfoils and compare time-averaged aerodynamic coefficients and lift-to-drag ratio at several angles of attack (i.e. 0 to 9 degrees).

# 3 Computational Methodology

## 3.1 Governing equations

The governing equations considered in the present study are the three-dimensional compressible Navier-Stokes equations. The system of governing equations is

$$\frac{\partial \rho}{\partial t} + \frac{\partial}{\partial x_k}\left(\rho u_k\right) = 0 \tag{1}$$

$$\frac{\partial}{\partial t}\left(\rho u_i\right) + \frac{\partial}{\partial x_k}\left(\rho u_i u_k + p\delta_{ik}\right) = \frac{1}{\mathrm{Re}_{a_\infty}}\frac{\partial \tau_{ik}}{\partial x_k} \tag{2}$$

$$\frac{\partial e}{\partial t} + \frac{\partial}{\partial x_k}\left(\left(e+p\right)u_k\right) = \frac{1}{\mathrm{Re}_{a_\infty}}\left(\frac{\partial u_l \tau_{kl}}{\partial x_k} + \frac{\partial q_k}{\partial x_k}\right) \tag{3}$$

where the viscous stress tensor, $\tau_{ij}$, and the heat flux, $q_k$, are given by, respectively,

$$\tau_{ij} = \mu\left[\left(\frac{\partial u_i}{\partial x_j} + \frac{\partial u_j}{\partial x_i}\right) - \frac{2}{3}\frac{\partial u_k}{\partial x_k}\delta_{ij}\right] \tag{4}$$

$$q_k = -\frac{\mu}{\left(\gamma-1\right)\mathrm{Pr}}\frac{\partial}{\partial x_k}\left(\gamma\frac{p}{\rho}\right) \tag{5}$$

All variables are non-dimensionalized by the chord length ($c$), the density ($\rho_\infty$), the dynamic viscosity ($\mu_\infty$) and the sound speed ($a_\infty$) of the free-stream. $Re_{a\infty}$ is defined as $(\rho_\infty a_\infty c)/\mu_\infty$. In the above equations, $\rho$ denotes the fluid density, $u_i$ the velocity component in the direction $x_i$, $p$ the static pressure, $e$ the total energy per a volume, $\mu$ the dynamic viscosity coefficient, and $Pr$ the flow Prandtl number assumed to be constant. The system is closed with the ideal gas equation of state written in the form

$$p = (\gamma - 1)\left( e - \frac{1}{2}\rho u_k u_k \right) \tag{4}$$

For all the flows considered in the present work, the specific heat ratio is set to $\gamma$= 1.4 and the Prandtl number to $Pr$= 0.72. In addition, the chord-and freestream-based Reynolds number is defined as $Re = Re_{a\infty}\, M_{a\infty}$ where the freestream Mach number $M_{a\infty}=U_\infty/a_\infty$.

## 3.2 Turbulence modelling

Present work employs the implicit LES approach and accounts for the unresolved small eddies by means of numerical dissipation. Thus no subgrid-scale model is employed and the unfiltered compressible Navier-Stokes equations are solved. This approach has been utilized to simulate the flow around several kinds of airfoils at low Reynolds numbers (for example, an SD7003 airfoil [8, 9], an NACA0012 airfoil [7, 10], an NACA0002 airfoil [7, 10], and Ishii airfoil [7, 10]).

## 3.3 Spatial and temporal discretization

The aforementioned equations are solved with LANS3D [11] developed in ISAS/JAXA. The spatial derivatives of convective terms, viscous terms, metrics, and Jacobian are computed by the sixth-order compact-differencing scheme [12]. In order to eliminate spurious components, the tenth-order low-pass spatial filtering [12, 13] is introduced with filtering coefficient of 0.495. Second-order backward differencing converged by symmetric alternating direction symmetric Gauss-Seidel scheme [14] is used for time integration. Furthermore depending on the flow fields around the airfoils from three to five inner iterations are introduced to obtain the converged solution each time-step [15].

Computational time step is set to be $0.00023c/a_\infty$ in non-dimensional time. The maximum local Courant-Friedrichs-Lewy number is approximately 1.6. At the outflow boundaries, all variables are extrapolated from one point inside of the outflow boundaries. On the airfoil surface, no-slip and adiabatic conditions are imposed. Periodic boundary condition is applied along with the spanwise direction in order to simulate an infinite wing. At the inlet boundaries, free-stream velocities are assigned without disturbances.

## 3.4 Grid sensitivity analysis and cross validation

In order to identify the sufficient grid resolution to capture the transition to turbulent that occurs in a separation bubble, we examine three different grids, a base grid with total 8 million, an intermediate grid with total 12 million, and a fine grid with 20 million points, see Figure 3. C-type structure mesh is used. The first cell away from

the wing surface is fixed for all test grids and set to be $0.03c/\sqrt{\mathrm{Re}}$. The distance from the wing surface to the outer boundary is 30*c*. The wing span-to-chord ratio is set to 0.2 following in the findings of our previous studies [10, 11] and Galbraith and Visbal [8].

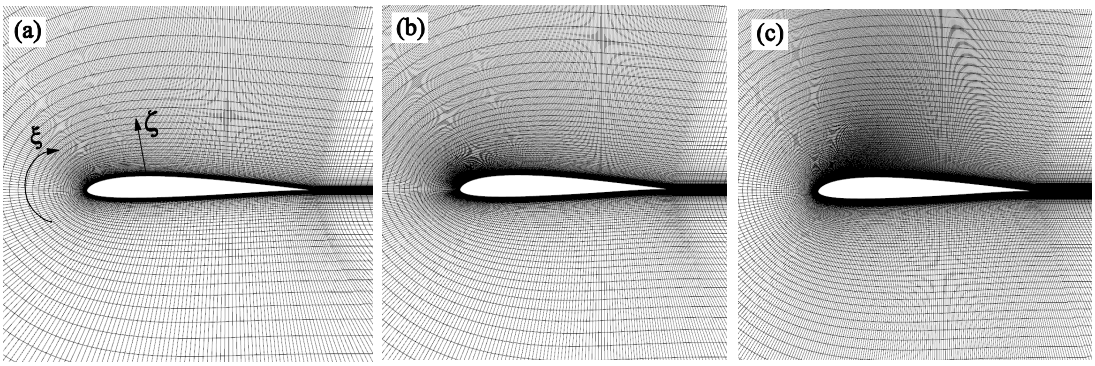


Figure 3: Tested grids: (a) coarse ($\xi\times\eta\times\zeta$: 488×201×80); (b) intermediate ($\xi\times\eta\times\zeta$: 615×201×101); (c) fine ($\xi\times\eta\times\zeta$: 775×201×127).

Figure 4 presents the averaged surface pressure and skin friction distributions for three tested grids and Figure 5 shows the wall-unit distribution of the intermediate grid. From the results shown in Figure 4 and Figure 5, the intermediate grid is selected and used for all simulations in present study. It should be mentioned that the intermediate grid satisfies the criterion ($\Delta\xi^+<25$, $\Delta\eta^+<15$, and $\Delta\zeta^+<1$) that are recommended for accurately performing turbulent analyses including near wall flow structure.

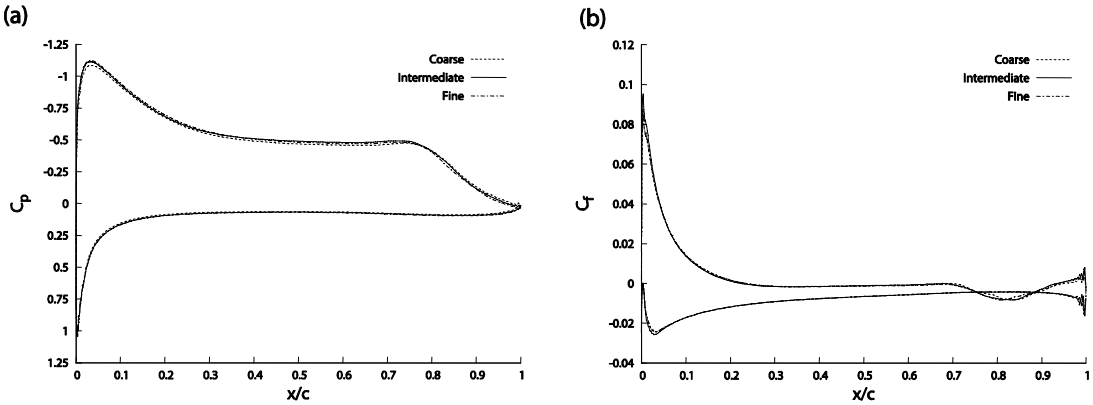


Figure 4: Averaged surface pressure and skin friction distributions for three tested grids. Dash, solid, and dash-dotted lines correspond to the coarse, intermediate, and fine grids, respectively.

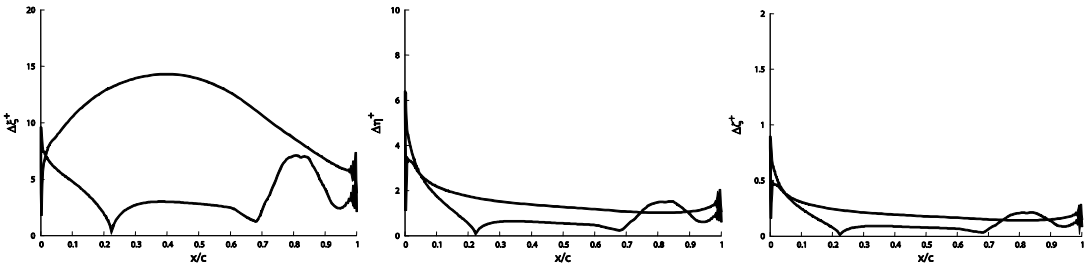


Figure 5: Grid-size distribution in the direction of chord of the intermediate grid around the SD7003 airfoil. Note $\Delta\xi^+$ is stream-wise grid spacing, $\Delta\eta^+$ is span-wise grid spacing, and $\Delta\zeta^+$ is wall-normal grid spacing. The superscript plus denotes the normalized value based on wall unit.

Because the experimental data of the SD7003 airfoil at several angles of attack at the Reynolds number considered in present study are not available, we compare the average surface pressure and skin friction distributions with the previous numerical result [9] for the similar case setup (AoA= 4° and $Re$= $2.2\times10^4$) as shown in Figure 6. The previous numerical result was obtained by solving the Equations (1), (2), and (3) using a high-order Discontinues Galerkin finite-element method with implicit LES approach [9]. As seen in Figure 6, current simulation qualitatively and quantitatively agrees well with previous numerical result.

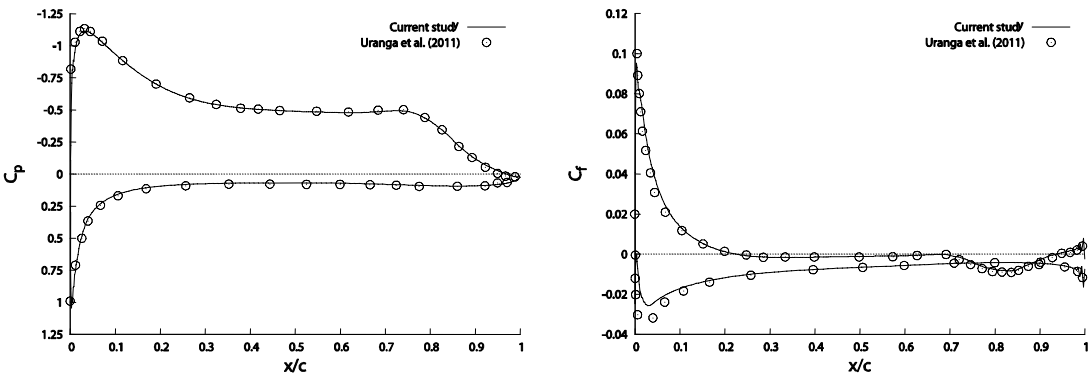


Figure 6: Averaged surface pressure (left) and skin friction (right) distributions as function of normalized chord length. The open circles are adopted from the numerical result of Uranga et al. [9]

# 4 Results and Discussions

## 4.1 Instantaneous flow fields

Figure 7 shows the instantaneous three-dimensional flow fields around the wings at specific angles of attack. Overall, instantaneous flow structures around three wings

at each angle of attack look qualitatively similar. Thus, we highlight common features and difference observed in instantaneous flow fields.

The difference of flow fields around the wings is clearly seen at the angle of attack of 3°. Although the flow past the Ishii wing shows two-dimensional coherent vortical structures in the wake, the flow around the SD7003 and the SD7003-Ishii wings presents formation and development of vortices in the suction side. The vortex structure observed in the suction side around the mid-span is a two-dimensional coherent vortex. Gradually it breaks down and forms hair-pin like vortical structure near the trailing edge (vortices are colored by red or blue in Figure 7). Common features can be seen in the flow near the leading edge and the process of vortex formation and development in the suction side of the wing. Especially, at high angles of attack the difference of the airfoil shape has little influence in the instantaneous flow structure around the wings due to the fully separated from the leading edge (e.g. AoA= 6° in Figure 7).

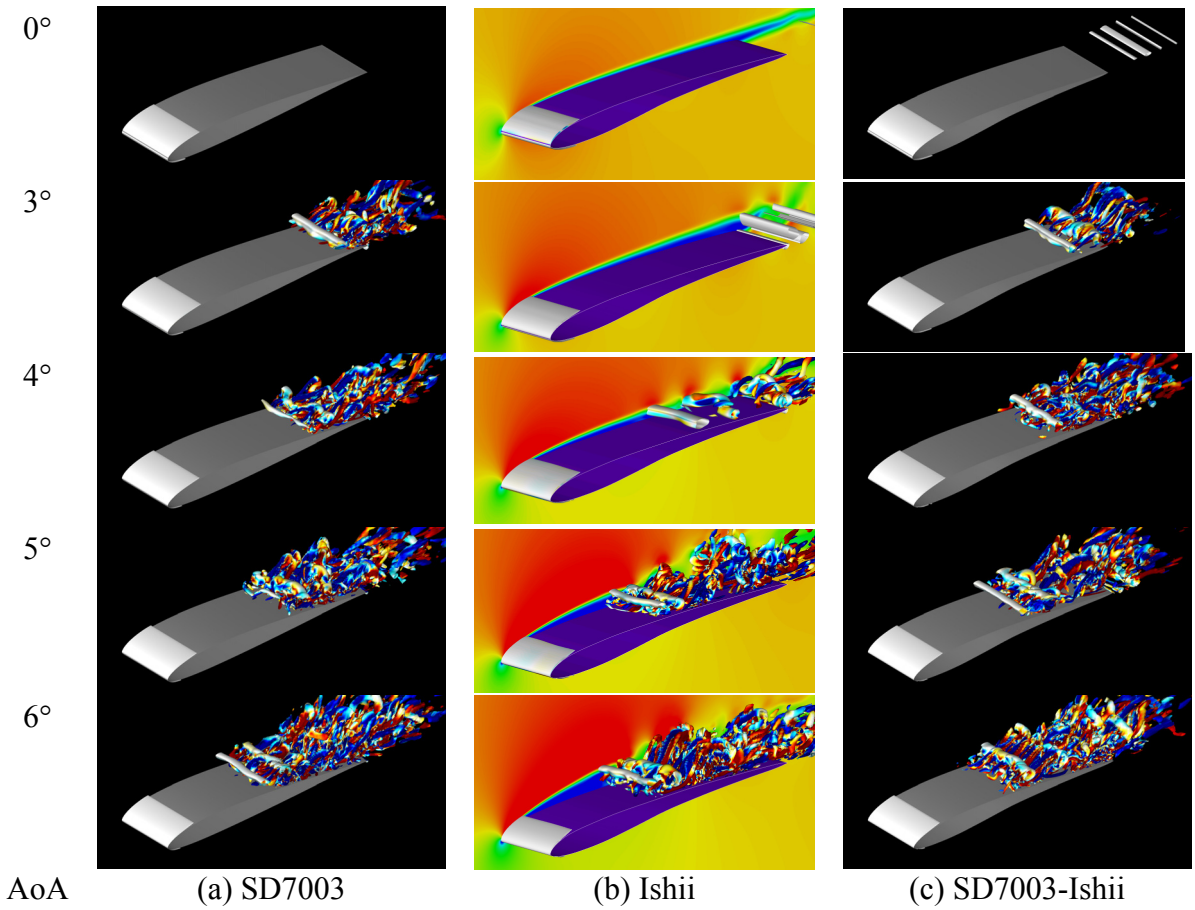


Figure 7: Snapshots of instantaneous flow fields around an SD7003, an Ishii, and an SD7003-Ishii wings. Iso-surfaces indicate the invariant of the velocity gradient (***Q***= 5) and its color shows streamwise vorticity (range: -5 to 5)

## 4.2 Averaged flow fields and surface pressure distributions

Figure 8 shows phase- and spanwise-averaged flow for several angles of attack with computed separation, transition, and reattachment points that are denoted as S, T, and R. Note that the average fields and surface skin friction and pressure distribution are computed by averaging the solution over a non-dimensional time of $50c/a_\infty$ and then performing a spatial average over all spanwise planes.

At the angle of attack of 0°, the flow attaches on all wings. When the angle of attack becomes 3°, the region where the flow separates around the SD7003 and the SD7003-Ishii wing (blue color region in Figure 8) is gradually expanded and moves toward the leading edge compared with those at low angles of attack. At the angle of attack of 4°, a long LSB is observed in the suction side of the wings. Moreover, it is clearly seen that larger and longer LSB existed on the suction side of the SD7003 and the SD7003-Ishii wings than that of the Ishii wing. From the angles of attack of 5° to 6°, the length of LSB of the SD7003 and the SD7003-Ishii wings reduce while that of the Ishii wing increases.

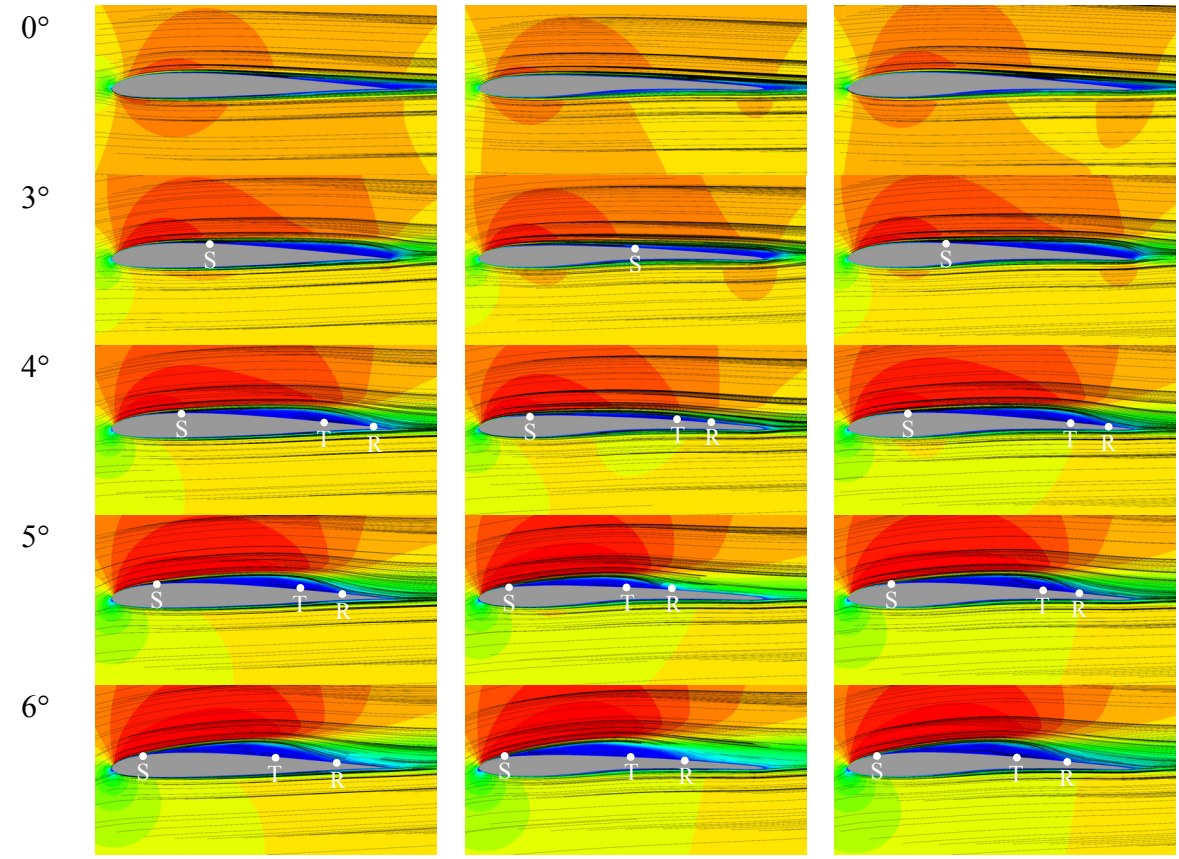


AoA (a) SD7003 (b) Ishii (c) SD7003-Ishii

Figure 8: Averaged stream-wise velocity contour and streamlines around three wings. Contour ranges from 0.0 to 0.25. Three points with notifications S, T, and R indicate the location of separation, laminar-to-turbulence transition, and reattachment point.

In order to gain further understanding of fluid physics including the LSBs, separation and reattachment, the surface pressure distributions are plotted in Figure 9 and Figure 10. It is noted that the locations of those points are estimated based on the averaged skin friction coefficient distribution. It shows that from the angle of attack of 4° up to 6° the LSBs are present for all wings. Furthermore all wings experience the laminar separation near the trailing edge at low angles of attack, the laminar separation at the leading edge and reattachment near the trailing edge (i.e. formation of the LSB) at intermediate angles of attack, and then the laminar separation at the leading edge at high angles of attack.

For all wings magnitude of suction peak increases with the angle of attack increases and similar peak values are observed. For the SD7003-Ishii wing, it is found that the averaged upper surface pressure distribution of the SD7003-Ishii wing are similar to that of the SD7003 airfoil as well as the averaged lower surface pressure distribution of the SD7003-Ishii wing are similar to that of the Ishii airfoil. This result implies that the change of airfoil cross-sectional shape does not significantly affect surface pressure distributions of each surface and the flow along with the lower surface. Furthermore, the length of the LSB decreases with the angle of attack increases up to 5°. However, the length of the LSB observed around the Ishii wing becomes similar to those observed in the SD7003 and the SD7003-Ishii wing because the location of reattachment point moves to trailing edge. This movement of reattachment point might be because the Ishii airfoil has flatter upper surface than that of the SD7003 airfoil. Similar dynamic behavior of the LSB is observed around the flat plate at the Reynolds number of $10^3$[16].

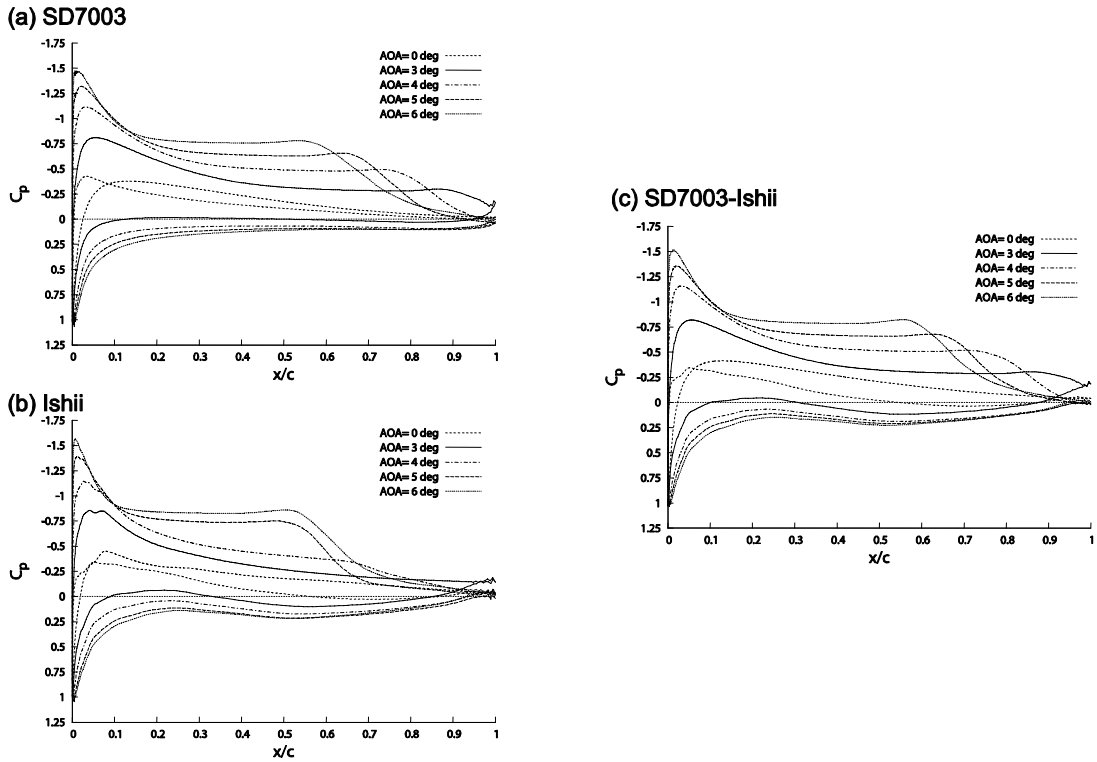


Figure 9: Phase- and spanwise-averaged surface pressure coefficient distribution for (a) the SD7003, (b) the Ishii, and (c) the SD7003 wings.

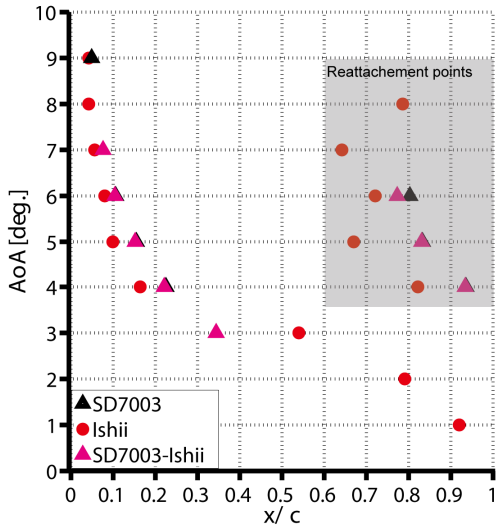


Figure 10: Location of computed separation and reattachment point.

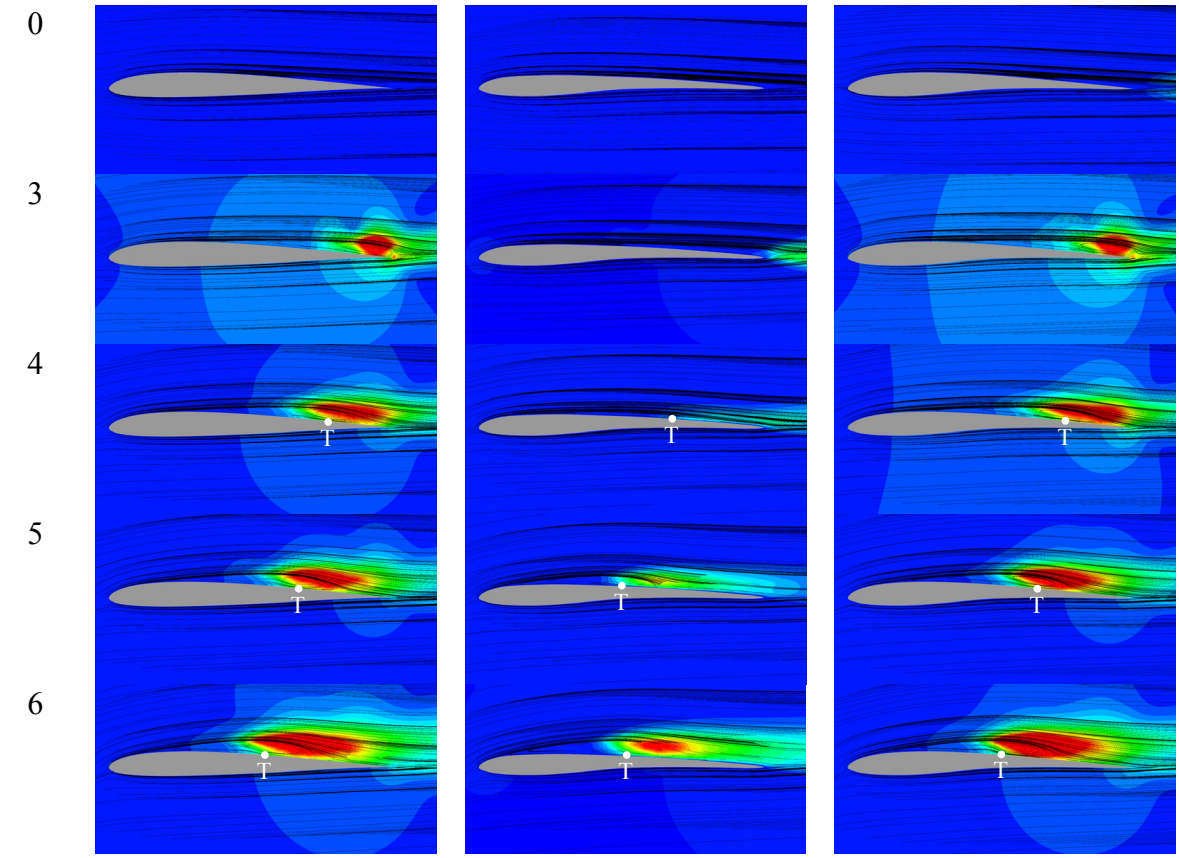


(a) SD7003 (b) Ishii (c) SD7003-Ishii

Figure 11: Phase- and spanwise-averaged turbulence kinetic energy and streamlines around three airfoils. T indicates the transition point.

Figure 11 shows the phase- and spanwise-averaged turbulence kinetic energy (TKE) distribution around the wings. The high TKE region corresponds to the position where the three-dimensional hairpin vortex is generated by the deformation of two-dimensional vortex (see Figure 7). After the transition occurs in the LSB high TKE region can be observed for the angle of attack of 4°, 5°, and 6°. This observation is consistent with the previous reports [1, 4]. As noted, the Ishii airfoil shows laminar-to-turbulent transition at higher angler of attack than the SD7003 airfoil one.

## 4.3 Averaged aerodynamic performances

The aerodynamic force coefficients as function of the angle of attack are plotted in Figure 12, Figure 13, and Figure 14. It should be noted that the angle of attack used in this study is the geometric angle of attack with respect to freestream and is not increment from the zero-lift angle of attack for each airfoil. From three figures several features are pointed out:

(i) the lower surface shape of the Ishii airfoil increases lift generation without increase of the drag;
(ii) the upper surface of the airfoil is a dominant factor for the drag generation at the angle of attack ranging between 0° and 5°;
(iii) the change in lift slope from the angle of attack of 3° to 4° is observed; and
(vi) at same angle of attack all wings attain maximum lift-to-drag ratio and the Ishii airfoil shows best performance in terms of the lift-to-drag ratio due to the smallest drag and medium lift.

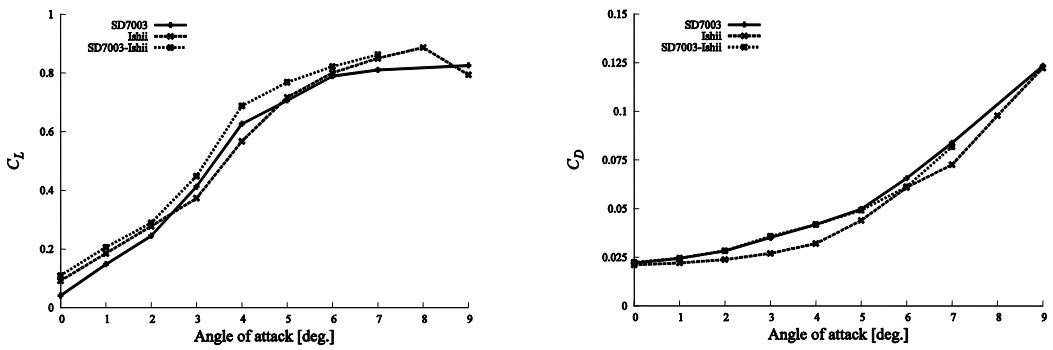


Figure 12: Mean lift (left) and drag (right) coefficients for three wings as function of angle of attack.

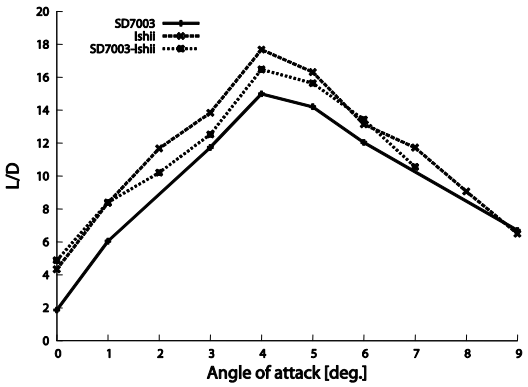


Figure 13: Lift-to-drag ratio of three wings against the angle of attack.

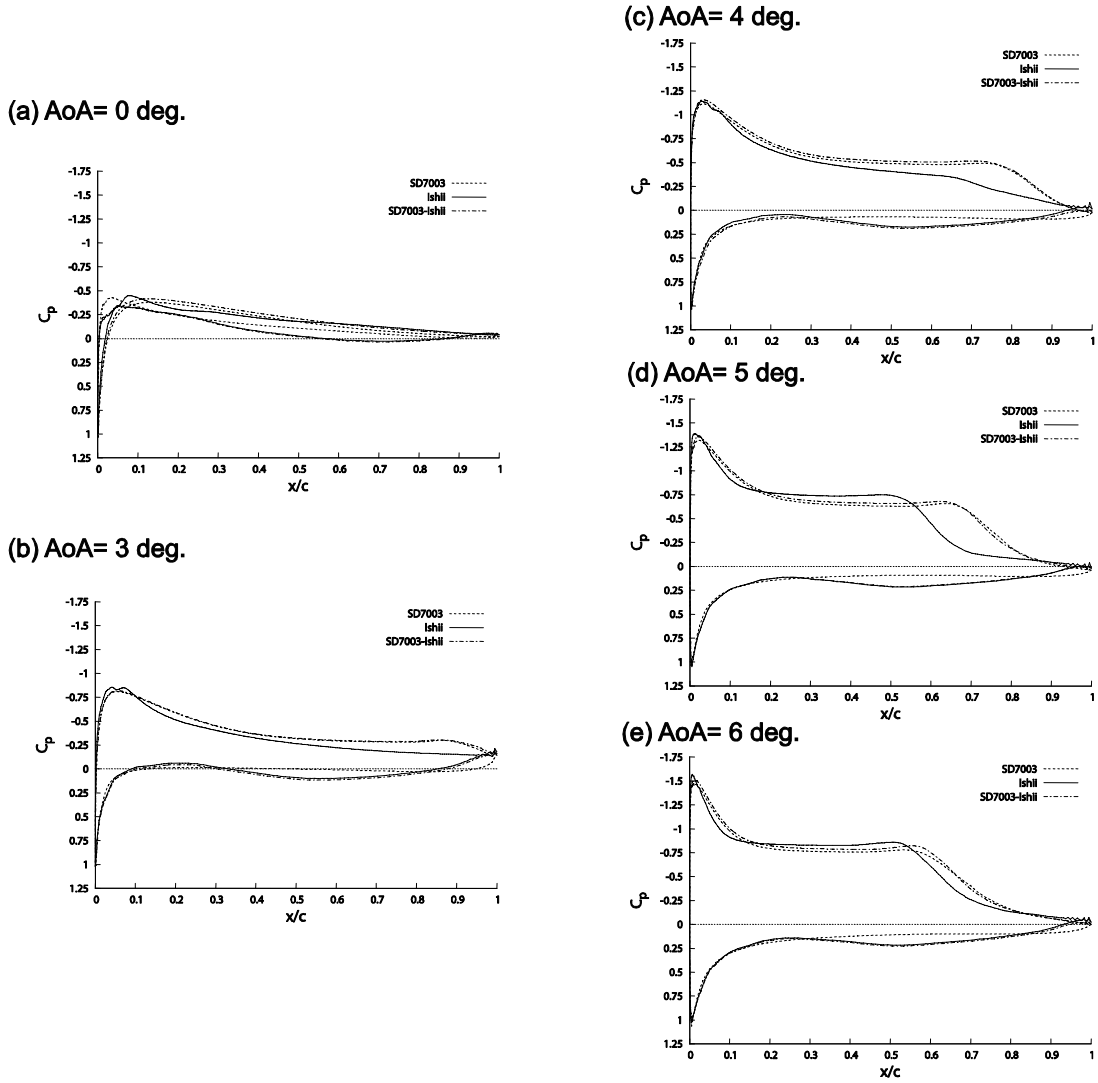


Figure 14: Comparison of phase- and spanwise-averaged surface pressure coefficient distribution: (a) AoA= 0°, (b) AoA= 3°, (c) AoA= 4°, (d) AoA= 5°, and (e) AoA= 6°.

Looking at the surface pressure distributions of the SD7003 and the SD7003-Ishii wing as shown in Figure 14, although the pressure distribution of upper surface of both airfoils are almost same including the region of plateau, the pressure distribution of lower surface are clearly different. This suggests that the greater positive curvature of the lower surface of the Ishii airfoil helps to increase lift generation. Note its influence is also observed in the pressure distribution near the trailing edge. Furthermore the reasons that the SD7003-Ishii wing generates largest lift at the angles of attack of 4° are 5° are the presence of longer LSB than that of Ishii wing and the positive camber of lower surface. In addition, the formation of the long LSB is strongly related to the point (iii) [10]. The characteristic of a long LSB is seen in the plateau of the pressure distribution at the angle of attack of 4°. It leads to increase not only in lift but also in drag.

# 5 Concluding Remarks

The effects of airfoil shape on low Reynolds number aerodynamics are numerically investigated. The flowfield around the wing is obtained by numerically solving Navier-Stokes equations. In order to compute unsteady turbulent flow with certain accuracy we perform the large-eddy simulations with $6^{th}$-order compact finite difference scheme and $10^{th}$-order low pass filter, and $2^{nd}$-order backward implicit time integration with inner iterations. Systematic numerical excesses show the feasibility of current simulations to predict flow fields around fixed-wing configurations involving a laminar separation and laminar-to-turbulence transition at low Reynolds number. At the Reynolds number of $2.3\times10^4$, two types of thin and asymmetric airfoils are considered. The results show that the upper surface of airfoil shape affects the formation of an LSB and the transition to turbulence in the three-dimensional flow around the wings and the lower surface of airfoil shape does not significantly affect the flow structures around the airfoil, however, it can help to increase lift generation if its shape is designed appropriately. Therefore significant influence in the aerodynamic performance is observed.

# References


[1] T.J. Mueller (ed.), “Fixed and Flapping Wing Aerodynamics for Micro Air Vehicle Applications”, American Institute of Aeronautics and Astronautics, Inc., Reston, VA, U.S.A., 2001.

[2] W. Shyy, Y. Lian, J. Tang, D. Viieru, H. Liu, “Aerodynamics of Low Reynolds Number Flyers”, Cambridge University Press, New York, NY, U.S.A., 2008.

[3] F. W. Schmitz, “The Aerodynamics of Small Reynolds Number”, NASA TM-51, 1980.

[4] P. B. S. Lissaman, “Low-Reynolds-Number Airfoils”, Annual Review in Fluid Mechanics, 15, 223-239, 1983.

[5] M.S. Selig, J.F. Donovan, D.B. Fraser, “Airfoils at Low Speeds”, Soartech 8, H.A. Stokely Publisher: Virginia Beach, VA, U.S.A., 1989.
[6] M.S. Selig, J.J Guglielmo, A.P. Groeren, P. Giguere, “Summary of Low-speed Airfoil Data”, Soartech Aero Publications, H.A. Stokely: Virginia Beach, VA, U.S.A., 1995.
[7] M. Anyoji, T. Nonomura, A. Oyama, K. Fujii, K. Nose, D. Numata, H. Nagai, K. Asai, “Aerodynamic Characteristics of Ishii Airfoil at Low Reynolds Numbers”, Proceeding of Eighth International Conference on Flow Dynamics, Sendai, Miyagi, Japan, 2011.
[8] M. C. Galbraith, M. R. Visbal, “Implicit Large-eddy Simulation of low Reynolds Number Flow Past the SD7003 Airfoil”, Forty-sixth AIAA Aerospace Sciences Meeting and Exhibit, Reno, NV, U.S.A., AIAA-2008-225, 2008.
[9] A. Uranga, P.-O. Persson, M. Drela, J. Peraire, “Implicit Large Eddy Simulation of Transition to Turbulence at Low Reynolds Numbers Using a Discontinuous Galerkin Method”, International Journal For Numerical Methods in Engineering, 87, 232-261, 2011.
[10] R. Kojima, T. Nonomura, A. Oyama, K. Fujii, “Computational Study of Flow Characteristics of Thick and Thin Airfoil with Implicit Large-eddy Simulation at Low Reynolds Number”, Proceedings of ASME-JSME-KSME Joint Fluids Engineering Conference 2011, Hamamatsu, Shizuoka, Japan, 2011.
[11] K. Fujii, S. Obayashi, “High-resolution upwind scheme for vortical-flow simulations”, Journal of Aircraft, 26, 1123-1129, 1989.
[12] S. K. Lele, “Compact Finite Difference Scheme with Spectral-like Resolution”, Journal of Computational Physics, 103, 16-22, 1992.
[13] D. V. Gaitonde, M. R. Visbal, “Pade Type Higher-order Boundary Filters for the Navier-Stokes Equations”, 38, 2103-2122, 2000.
[14] H. Nishida, T. Nonomura, “ADI-SGS Scheme on Ideal Magnetohydrodynamics”, Journal of Computational Physics, 228, 3182-3188, 2009.
[15] S. R. Chakravarthy, “Relaxation Methods for Unfactored Implicit Upwind Schemes”, twenty-second Aerospace Sciences Meeting, Reno, NV, U.S.A., AIAA-84-0165, 1984.
[16] M. Anyoji, “Development of a Mars Wing Tunnel and Its Applications to Low Reynolds Number and High-subsonic Airfoil Testing”, Ph.D dissertation, Tohoku University, Japan, 2011.